Optics Letters

Optically levitated conveyor belt based on polarization-dependent metasurface lens arrays

Feng Xu,[1,2] Yang Liu,[1,2] Chi Zhang,[1,2] Min Jiang,[3] Jiahui Zhang,[1,2] Guanghui Wang,[1,2,*] Fei Xu,[1] and Yanqing Lu[1]

[1]College of Engineering and Applied Sciences, Nanjing University, Jiangsu 210093, China
[2]Key Laboratory of Intelligent Optical Sensing and Integration of the Ministry of Education, Nanjing University, Jiangsu 210009, China
[3]Wuxi University, Jiangsu 214105, China
*Corresponding author: wangguanghui@nju.edu.cn

Received 3 March 2022; revised 23 March 2022; accepted 23 March 2022; posted 25 March 2022; published 19 April 2022

In this Letter, we have proposed an optically levitated conveyor belt based on periodic arrays of a polarization-dependent nanoslit-based metasurface lens (NBML) that is capable of realizing far-field capture, transport, and sorting. The NBML in arrays can be lit up in a relay way by rotating the polarization angle of the excitation beam and thereby provide a better stiffness for transporting particles. When excited at the wavelength of 1064 nm and power density of 0.3 mW/μm^2, the particles will follow the directional movement of hot spots with an alternative switch of polarization angle and the success ratio of transport can be up to 97.0% with the consideration of Brownian motion. Furthermore, the influence of polarization switching time and incident optical power densities on the efficiency of transport are investigated numerically from a statistical point of view. The sorting of particles with different sizes has also been proved in a given power density. With the analysis of numerical results, our research provides a new approach, to the best of our knowledge, for particle trapping and transport, which is beneficial to on-chip optofluidic applications.

https://doi.org/10.1364/OL.457314

Optical tweezers (OTs) refers to a method that utilizes the optical gradient force formed by focusing a mode field (e.g., hot spots) to trap or manipulate particles [1]. Because of the advantages in biomedical fields, such as sub-wavelength cell trapping [2], single-cell motion [3], etc. [4,5], OTs have drawn a great deal of attention in the past decades. Traditional methods that can form OTs usually rely on focusing spots with diffraction [6]. However, the possibility of sample damage resulting from heat generation cannot be negligible, because sufficient power density is required to form gradient force to capture particles. In addition, the position of trapped particles cannot be determined accurately and the conventional diffraction-limited architecture will also confine realistic applications. Therefore, plasmatic metasurfaces and waveguides have been widely researched owing to the localized evanescent wave, which can confine the particles to the surface of nanostructures and further the area of hot spots [7–9]. In order to realize the delivery of micro- or nanoparticles, researchers use the directional movement of hot spots to manipulate the transport of particles. Wang *et al.* [10] successfully rotated nanoparticles with manual rotation of incident linear polarization in 2011. Hansen *et al.* [11] designed C-shape arrays that can transport particles with the change of polarization direction and wavelength. In addition, several polarization-dependent plasmonic structures have been designed and the distribution of particles has been analyzed from the perspective of statistics in recent years [12–14]. However, near-field hot spots cannot guarantee most of the particles suspended will be effectively trapped and transported to the next hot spots of the nanostructures because near-field electrical strength will decrease quickly.

Particle manipulation in the far field is a promising way to reduce the disadvantages mentioned above. In recent years, particle trapping in the far field with photonic nanojets (PNJs) [2] and metalenses [15,16] have been researched because of the greater performance of trapping, especially for particles suspended in a liquid environment. However, researches on transporting particles in the far field, just like the motion type of magnetically levitated trains, have not been demonstrated. Many methods that can form far-field focusing owing to phase match, such as the metasurface planer lens [17] and dielectric metalens [18], have been widely studied in past years, so we can take advantage of these structures to achieve far-field transport.

In this Letter, a nanoslit-based metasurface lens (NBML) that satisfies the condition of phase match is applied so that far-field focusing can be obtained and enhanced. By manipulating the polarization angle, the directional movement of hot spots can be realized. Simultaneously, polystyrene (PS) particles will follow the path of hot spots because of the provided gradient force of mode fields. Furthermore, Brownian motion in an aqueous solution has been considered along with the transport process in order to simulate the distribution of particles statistically and accurately. Different power densities and polarization switching times have also been analyzed for the most suitable parameters of pumping light. In addition, particle sorting has also been demonstrated numerically.

As shown in Fig. 1(a), three kinds of permutations of NBML in circulation are consisted in the optically levitated conveyor belt and a structure period is composed with three orientated NBMLs. The channel is filled with de-ionized water over the

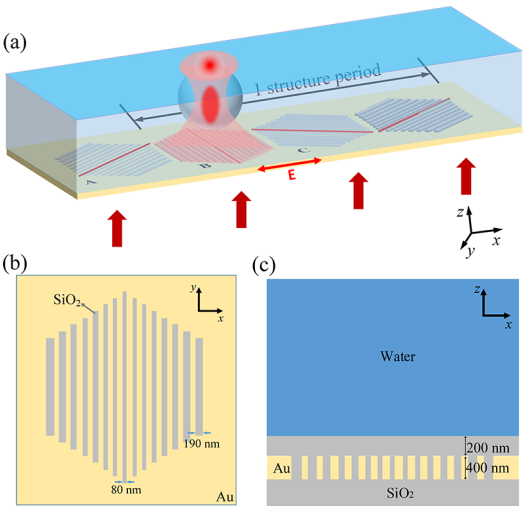

Fig. 1. (a) Schematic diagram of an optically levitated conveyor belt irradiated by incident polarized light. The red dual-arrow represents the polarization direction. (b) Vertical view of the NBML consisting of 15 nanoslits. (c) Front view of the NBML.

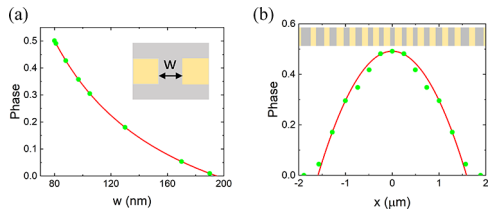

Fig. 2. (a) Function of phase delay and the width between the two nanoslits w (solid line). The dots indicate the widths used in our design. (b) Phase delay introduced by nanoscale slits (dots) and the difference from theoretical curves (solid line).

structure and the PS particles will be suspended in the fluid channel. The incident light is radiated under the nanostructure. A–C represent the oblique right, vertical, and oblique left directions, respectively and their interval is 4.5 μm. Figures 1(b) and 1(c) show the x–y and x–z planes of the NBML. Considering a single NBML, 15 nanoslits symmetrical to the middle nanoslit are inset into a 400-nm golden layer and filled with silica. We have changed the shape of the NBML from a rectangle to a quasi-hexagon, which is convenient for our arrangement of arrays. The length of the middle nanoslit is 5 μm and the marginal nanoslits have been reduced to 2.55 μm gradually. In order to protect the surface of the Au, a 200-nm silica layer is also used as a coating, as shown in Fig. 1(c), which will have nearly no effect on the optical mode field.

We firstly characterize the parameters and optical mode field by considering a single NBML (i.e., the 15 nanoslits compose a unit cell). Figure 2(a) derives the relationship between the phase delay and the width of the nanoslits, which satisfies the following [19]:

$$\tanh\left(\frac{w}{2}\sqrt{\beta^2 - k_0^2\varepsilon_1}\right) = -\frac{\varepsilon_1\sqrt{\beta^2 - k_0^2\varepsilon_2}}{\varepsilon_2\sqrt{\beta^2 - k_0^2\varepsilon_1}}, \tag{1}$$

where w represents the width of the nanoslits, ε_1 and ε_2 denotes the permittivity of water and metal, respectively, k_0 is the free space propagation constant, β is the propagation constant of the

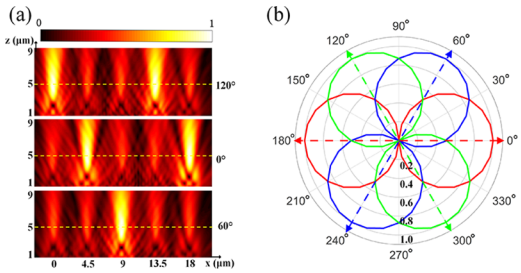

Fig. 3. (a) Normalized electric field distribution when the angle of polarized incident light is 120°, 0°, and 60°. The dotted lines denote the location of $z = 5$ μm. (b) Normalized statistical intensity of electric field intensity of different orientated NBMLs corresponding to A (green line directed to 120°), B (red line directed to 0°), and C (blue line directed to 60°) in Fig. 1(a) under different angles of polarization.

metasurface lens, and the phase delay of a single nanoslit can be expressed as $\varphi = \beta d$, where d is the thickness of the metal film. With the increase of the width of the nanoslits, the phase delay will reduce because narrower slits will make a greater part of the mode reside in the layer of metal, so that the light will travel more slowly and more phase delay will be introduced.

In addition, the phase delay caused by propagations in water should also be considered. The function of distance x from the center of the lens and phase delay can be predicted as follows [19]:

$$\varphi(x) = C + \frac{2\pi n f}{\lambda} + \frac{2\pi n\sqrt{f^2 + x^2}}{\lambda}, \tag{2}$$

where λ represents the wavelength of incident light—1064 nm is selected in our design for low thermal effect, n is the refractive index of water, and f denotes the focal distance of the lens. As shown in Fig. 2(b), the realistic points deviate from the theoretical curves a little because F-P oscillations will occur in the slots. Moreover, the transmission will vary with the width of the slits and the amplitude modulation may do damage to our phase matching.

In order to verify the change of mode field when the incident polarization direction varies, we have simulated the electrical field distributions by the finite-difference time-domain (FDTD) method with a plane wave exerted from below the substrate. As shown in Fig. 3(a), when the polarization direction is perpendicular to the symmetry axis of the NBML, only one oriented NBML can be excited and the electrical mode field will be enhanced much more than the other. The dotted line indicates the location of $z = 5$ μm, where the intensity is almost the strongest and we have chosen to transport particles at such a height. Moreover, when the polarization direction is rotated in the regular method, the lit host spots will move forward gradually, which can be used for particle trapping and transport. We have also analyzed the normalized intensity of different orientation NBMLs under different polarization directions statistically, as shown in Fig. 3(b). Their characteristics are consistent and the intensity of the other two kinds of NBMLs can only achieve ~50% intensity compared with the excited one. The localized enhancement will provide the pedestal and better stiffness for our trapping and transporting.

When we locate the 6-μm PS sphere at $z = 5$ μm initially and then calculate the gradient forces exerted on it with the volumetric technique, several results can be obtained, shown as dots in Fig. 4(a), and the line is achieved by curve fitting with the

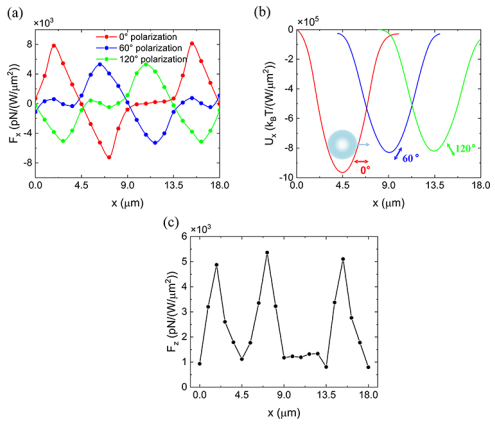

Fig. 4. (a) F_x and (b) trapping potential well when the light is exerted on a 6-μm PS sphere under 0° (red line), 60° (blue line), and 120° (green line) polarization directions, respectively. (c) Function of F_z and x under 0° polarization. The dots denote the number calculated with the FDTD.

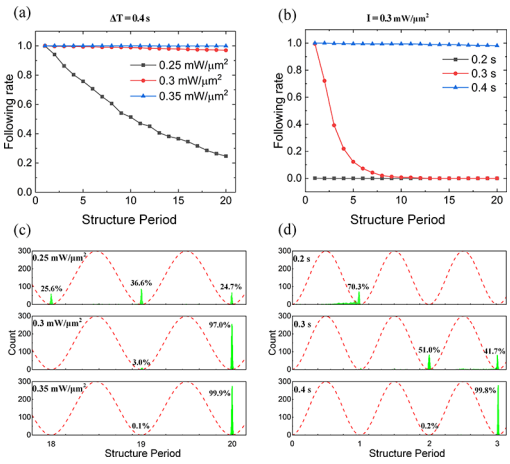

Fig. 5. Analysis of the transport within 20 structure periods (each structure period corresponds a switching period that consists of $3\Delta T$). (a) When ΔT is 0.4 s, the following rate with the increase of switching period irradiated by 0.25 mW/μm² (squares), 0.3 mW/μm² (circles), and 0.35 mW/μm² (triangles). (b) When I is set as 0.3 mW/μm², the function of the following rate and switching period when ΔT is 0.2 s (squares), 0.3 s (circles), and 0.4 s (triangles). (c) Particle distributions when 20 switching periods have been experienced with different I. (d) Particle distributions when three switching periods have been experienced with different ΔT. The dotted lines in (c) and (d) are used to simulate the potential wells when 120° polarization is set. The numbers in the figure show the rate of the particles located in the bottom of the corresponding potential wells.

signed dots. The potential well can be calculated by integrating Fx along x direction, as shown in Fig. 4(b). The bottoms of potential well correspond to the locations where Fx is zero. With the rotating of the polarization direction, the bottom of the potential well will also move forward gradually. If particles are assembled in the bottom of 0° polarization currently, they will be attracted to the next bottom of potential well when 60° polarization is applied and continuously the potential bottom of 120° polarization. In addition, the particles will not trace backwards because three polarization directions are applied. Figure 4(c) shows the forces suffered in the z direction under 0° polarization. The forces are positive, which means the force received by the particles will always be upward and the particles cannot remain suspending in the de-ionized water. Therefore, a cover plate should be used at the top of the fluid channel, which is shown with the blue flat in Fig. 1(a), to avoid the movement in the z direction.

We have simulated cases of particle transport within 20 switching periods with different I and ΔT, as shown in Fig. 5, with Einstein's Brownian motion theory [14,19]. Every switching period includes the time of $3\Delta T$. In order to judge the efficiency of particle transport, the number of particles attracted to the next lit hot spots when the polarization direction is rotated should be calculated. Therefore, the following rate, expressed as the rate of numbers transported to the target position to the sum of particles, has been defined to express such a target where the sum of particles N is fixed as 1000 in our calculations. When Δt is fixed as 0.4 s, different I of 0.25 mW/μm², 0.3 mW/μm², and 0.35 mW/μm² are investigated in Fig. 5(a). When I is only 0.25 mW/μm², the following rate will decrease quickly with the increase of switching period because a lower I cannot provide enough gradient force for particles to jump to the next potential well when polarization is rotated. When I is over 0.3 mW/μm², the following rate will always maintain a high level. Therefore, 0.3 mW/μm² is used to investigate the effect of polarization switching time to the following rate, as shown in Fig. 5(b). For the cases of 0.2 s and 0.3 s, the following rate is down to 0 in only a few periods, while 0.4 s can effectively keep the following rate at ~1, which indicates that the particle motion can stably follow the change of potential well. Therefore, the ultimate switching time of polarization will be set as 0.4 s.

As shown in Fig. 5(c), when 20 switching periods are finished, the distribution of particles with different I is shown. Most of the particles are located at the bottom of the potential well (the bottom of the dotted lines). For the cases of 0.3 mW/μm² and 0.35 mW/μm², 97 and 99.9% particles can transport to the target location and the remaining particles only fall behind one structure period. Therefore, if one or two more switching periods of polarization undergone, the following rate can be up to even 100%. When 0.25 mW/μm² is fixed, only 24.7% particles can successfully transport to the designated area and about half have a delay of at least two structure periods. When $\Delta T < 0.4$ s, the following rate will decrease sharply, so we only give the distributions in the first three potential wells at the third switching period of polarization rotation, as shown in Fig. 5(d). Most of the particles can be transported to the target area only when $\Delta T = 0.4$ s, which agrees with the results of Fig. 5(b).

In realistic application, a low I is required because the thermophoretic effect will be more significant under high power. Therefore, we have also investigated the possibility of transport under a lower power than 0.3 mW/μm² numerically. When the following rate can reach up to 99%, the switching periods needed for polarization rotation as a function of I are as shown in Fig. 6(a). When $I = 0.25$ mW/μm², only four additional switching periods are required for effective transport. For the case of around 0.2 mW/μm², many additional switching periods are needed. However, for scenarios with relatively small time requirements, these powers are also options. In order to show the evolution of particle distributions after additional switching periods, 0.225 mW/μm², which needs 14 additional switching periods, is selected and three intermediate processes are shown in Fig. 6(b). All of the particles have a delay of at least five

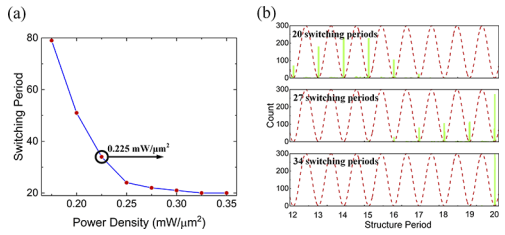

Fig. 6. (a) Switching periods required to transport particles to the target position under different I. (b) Particle distributions when 20, 27, and 34 switching periods have been experienced when $I = 0.225\ \mathrm{mW/\mu m^2}$, which is shown in (a). The dotted lines in (b) are used to simulate the potential wells when 120° polarization is set.

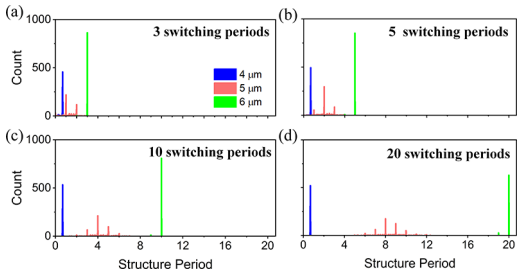

Fig. 7. Distribution of particles with 4 μm (the left blue histogram), 5 μm (the middle red histogram), and 6 μm (the right green histogram) when (a) three switching periods, (b) five switching periods, (c) 10 switching periods, and (d) 20 switching periods have been experienced. Here, I is fixed as $0.3\ \mathrm{mW/\mu m^2}$.

structure periods when 20 switching periods are experienced and 62.4% of particles have arrived at the target area after an additional seven switching periods. After 34 switching periods, almost all of the particles will be assembled at the designated structure period.

The distribution of particles with different sizes has also been investigated numerically, which can be used to sort particles, as shown in Fig. (7); $I = 0.3\ \mathrm{mW/\mu m^2}$ and $\Delta T = 0.4$ s are used in such cases. The distributions of particles with different sizes vary very much because the optical forces exerted on 6-μm particles can effectively push the particles forward, while the forces will not be enough with 4-μm and 5-μm particles. Therefore, with the increase of switching periods, the mean position of particles with different sizes will get farther and farther away, but 4-μm and 5-μm particles will lag behind the target area more and more. As shown in Fig. 7(a), three sizes of particles still have a great degree of coincidence when three switching periods are experienced. In order to show the difference between the mean locations, we have also calculated that the average velocities for 4-μm, 5-μm, and 6-μm particles are 0.44 μm/s, 4.61 μm/s, and 11.10 μm/s, which obviously shows that 4-μm particles have barely moved while 6-μm particles can almost catch up with the velocity of the hot spots change. Therefore, if 20 switching periods are applied, only 6-μm particles will be propitiously transported to the target area. Furthermore, we can also separate the particles with different sizes in different locations of the fluid channel so that we can realize the transport and sorting simultaneously.

In conclusion, we have designed an optically levitated conveyor belt based on NBML arrays that can be selectively lit up with different polarization directions of the light source. The structure can provide better stiffness for particle transport under low-incident power intensity. We have analyzed the following rate and particle distributions when different power intensities and polarization switching times are applicated. Furthermore, the possibilities of effective transport under lower power have also been investigated. Finally, we also prove that the transport and sorting of particles with different sizes can be realized simultaneously after several switching periods. Our investigations have a great prospect for applications in the fields of microorganism manipulation in microfluidic systems and on-chip optofluidic use.

Funding. National Natural Science Foundation of China (61875083, 61535005); Social Development Project of Jiangsu Province (BE2019761).

Disclosures. The authors declare no conflicts of interest.

Data availability. Data underlying the results presented in this paper are not publicly available at this time but may be obtained from the authors upon reasonable request.

REFERENCES

1. A. Ashkin, J. M. Dziedzic, J. E. Bjorkholm, and S. Chu, Opt. Lett. **11**, 288 (1986).
2. Y. Li, H. Xin, X. Liu, Y. Zhang, H. Lei, and B. Li, ACS Nano **10**, 5800 (2016).
3. T. L. Min, P. J. Mears, L. M. Chubiz, C. V. Rao, I. Golding, and Y. R. Chemla, Nat. Methods **6**, 831 (2009).
4. A. Ashkin and J. M. Dziedzic, Science **235**, 1517 (1987).
5. S. M. Block, L. S. B. Goldstein, and B. J. Schnapp, Nature **348**, 348 (1990).
6. D. G. Kotsifaki and S. N. Chormaic, Nanophotonics **8**, 1227 (2019).
7. Y. Zhao, A. A. E. Saleh, and J. A. Dionne, ACS Photonics **3**, 304 (2016).
8. W. Zhang, Y. Zhang, S. Zhang, Y. Wang, W. Yang, C. Min, and X. Yuan, Opt. Express **29**, 11664 (2021).
9. G. B. Loozen and J. Caro, Opt. Express **26**, 26985 (2018).
10. K. Wang, E. Schonbrun, P. Steinvurzel, and K. B. Crozier, Nat. Commun. **2**, 469 (2011).
11. P. Hansen, Y. Zheng, J. Ryan, and L. Hesselink, Nano Lett. **14**, 2965 (2014).
12. G. Wang, Z. Ying, H. Ho, Y. Huang, N. Zou, and X. Zhang, Opt. Lett. **41**, 528 (2016).
13. M. Jiang, G. Wang, W. Xu, X. Xu, W. Ji, N. Zou, and X. Zhang, Opt. Lett. **44**, 53 (2019).
14. C. Zhang, M. Jiang, Y. Chang, Y. Liu, G. Wang, F. Xu, and Y. Lu, Opt. Lett. **46**, 1522 (2021).
15. J. Hong, X. Zhou, R. Zhuang, W. Peng, J. Liu, A. Liu, and Q. Wang, Chin. Opt. Lett. **20**, 023601 (2022).
16. M. Hen, S. Ivan, H. Netta, and G. Pavel, Nano Lett. **18**, 5024 (2018).
17. Y. Zhu, W. Yuan, W. Li, H. Sun, K. Qi, and Y. Yu, Opt. Lett. **43**, 206 (2018).
18. T. Chantakit, C. Schlickriede, B. Sain, F. Meyer, T. Weiss, N. Chattham, and T. Zentgraf, Photonics Res. **8**, 1435 (2020).
19. L. Verslegers, P. B. Catrysse, Z. Yu, J. S. White, E. S. Barnard, M. L. Brongersma, and S. Fan, Nano Lett. **9**, 235 (2009).